

Lévy Defects in Matrix-Immobilized J Aggregates: Tracing Intra - and Inter-Segmental Exciton Relaxation

-SUPPORTING INFORMATION-

Larry Lüer^{*a}, Sai Kiran Rajendran^{b,c}, Tatjana Stoll,^b Lucia Ganzer,^b Julien Rehault^{b,d}, David M. Coles^e,
David Lidzey^e, Tersilla Virgili,^b and Giulio Cerullo^b

a) IMDEA Nanociencia, C/Faraday 9, 28049 Cantoblanco (Madrid), Spain, * larry.luer@imdea.org

b) IFN-CNR, Dipartimento di Fisica, Politecnico di Milano, Piazza L. da Vinci 32, 20133 Milano, Italy

c) School of Physics and Astronomy, University of St. Andrews, St. Andrews, Fife, KY16 9SS (UK)

d) Paul Scherrer Institut, 5232 Villigen PSI, Switzerland

e) University of Sheffield, Department of Physics and Astronomy, Sheffield S3 7RH (UK)

TABLE OF CONTENTS:

- A Calculation of exciton states in linear J aggregates with heavy tail states**
- B Calculation of linear absorption and 2DES maps**
- C Comparison of models**
- D Complete results of global fitting**
- E Pump intensity dependence**
- F Details of experimental method**

A Calculation of exciton states in linear J aggregates with heavy tail states

We consider the single TDBC molecules as two-level systems. Our J aggregate is formed by linearly aligning N of such molecules such that in a Cartesian coordinate system, the position of the nth molecule is [x_n; 0; 0]. In the basis of the molecular states |0⟩ and |n⟩ (all molecules in electronic ground state and nth molecule in excited state, respectively), the Frenkel Hamiltonian reads as

$$H = \sum_n^N \epsilon_n B_n^\dagger B_n + \sum_{n,m=1; n \neq m}^N J_{nm} B_m^\dagger B_n \quad (S1)$$

Here, B_n^\dagger is the creation operator acting on molecule n such that $B_n^\dagger|0\rangle = |n\rangle$ and $B_n^\dagger|n\rangle = |0\rangle$, because it is a two-level molecule, where excitations behave as bosons. Conversely, B_n is the annihilation operator for molecule n acting as $B_n|0\rangle = |0\rangle$ and $B_n|n\rangle = |0\rangle$. The parameter ϵ_n denotes the monomer transition energy between |0⟩ and |n⟩, while J_{nm} denotes the coupling between the molecular transitions at sites n and m, causing excitonic interaction. Note that we

explicitly consider non-nearest neighbor couplings, which is important to correctly calculate transitions between the one-and two-exciton bands that cause the induced absorption contribution to the two-dimensional spectra (see Fig.1 of main text). Note also that we neglect biexciton stabilization, i.e. we only consider the coupling between singly excited states on the aggregate.¹

Diagonal disorder is induced into the Hamiltonian in the following way: for a given aggregate of N monomers, we pick the site energies ϵ_n from a set of normally distributed random numbers. The coupling parameters J_{nm} are calculated from the distance $R_{n,m}$ of monomers n and m using the point-dipole approximation:

$$J_{nm} = k_e \left[\frac{(\mu_n \cdot \mu_m)}{|R_{n,m}|^3} - 3 \frac{(R_{n,m} \cdot \mu_n) \cdot (R_{n,m} \cdot \mu_m)}{|R_{n,m}|^5} \right] \quad (S2)$$

with $k_e = (4\pi\epsilon_r\epsilon_0)^{-1}$, where $\epsilon_0 = 8.854 \times 10^{-21} \text{ F/nm}$ is the dielectric constant in vacuum, and $\epsilon_r = 3$ has been assumed for the relative permittivity. The molecular transition dipole moments $\mu_i = \mu_j = [1.869 \times 10^{-20} \text{ Cm}; 0; 0]$ are given as vectors in Cartesian coordinates. For pure diagonal Gaussian disorder, the position of the aggregate in space is given by $\{R_1 = [0,0,0]; R_{n,n+1} = [1.0 \text{ nm}; 0; 0] \text{ for } n \in \{1; \dots; N-1\}\}$. These numbers were chosen such as to reproduce the experimental red shift of the J aggregate band against the monomer transition.

Off-diagonal disorder is introduced in the following way: We randomly picked a set of N_{tr} trap positions $t_j; j \in \{1; 2; \dots; N_{tr}\}; t_j \in \{1; 2; \dots; N\}$ along the chain and increased the nearest-neighbor distance at these positions to $R_{t_j, t_{j\pm 1}} = [\pm 1.2 \text{ nm}; 0; 0]$. Example: a choice of $t_j = \{3; 8\}$ on a 10-mer (corresponding to $N_{tr}=2; N=10$) would cause the x coordinates of the monomers to be at $x_n = \{0; 1.0; 2.2; 3.4; 4.4; 5.4; 6.4; 7.6; 8.8; 9.8\}$. Our two traps have thus increased the total length of the 10-mer by 0.8 nm, because the extra distance of 0.2 nm has been applied to the left and to the right at both trap positions. As eq. (S2) is a sharp function of distance, applying an extra distance of only 0.2 nm causes a substantial drop of the intermolecular couplings, leading to an effective segmentation of the aggregate chain. A typical realization of diagonal and off-diagonal disorder can be found in Fig. 1b and c, respectively. Within our model the nearest neighbor couplings $J_{n, n\pm 1}$ can adopt two different values, the “ideal one” and a largely reduced one in the vicinity of the defects. This is an extreme representation of a “heavy tailed” distribution in the sense that the reduced values of $J_{n, n\pm 1}$ in the neighborhood of a trap constitute the “tail” of the (delta-like) distribution of the majority of ideal coupling strengths.

For ensemble averaging, we calculated 500 realizations of such aggregates and diagonalized the resulting Hamiltonians using the QuTIP package,² restricting the solution space to singly (for simulation of linear absorption spectra) and up to doubly (for simulation of 2DES maps) excited aggregates using excitation number restricted operators. The resulting eigenstate coefficients c_{em} for the singly excited excitonic states e , in the basis of the molecular eigenstates, define the one- exciton wavefunctions:

$$\Psi_e = \sum_m c_{em} B_m^\dagger |0\rangle \quad (S3)$$

while the two-exciton wavefunctions are defined as:

$$\Phi_f = \sum_{kl}^{k>l} C_{f,kl} B_k^\dagger B_l^\dagger |0\rangle \quad (S4)$$

Note that although the two-exciton coefficients in eq. (S4) carry three indices f , k , and l , they still address elements of the 2D matrix of eigenstate coefficients from the diagonalization of the Hamiltonian, only that in the case of two-excitons, the corresponding doubly excited states (a single column in the C matrix) carry two indices, indicating which molecular excitations are involved.

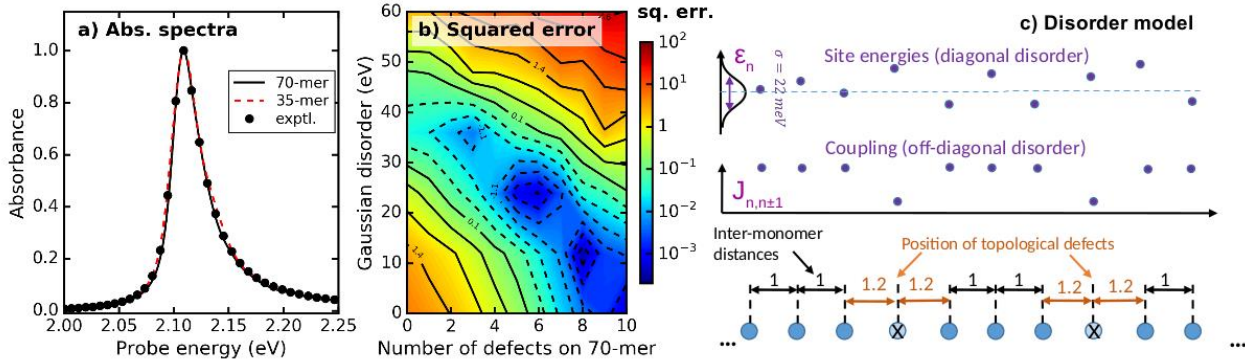


Figure S1. a) . (a) Ground state absorption spectrum (dots) and best fit (solid and dashed line for 70-mer and 35-mer, respectively). b) b) squared error (in a logarithmic color scale) between simulated and experimental GSA spectra as function of the width of the Gaussian distribution of site energies and the number of defects on a 70-mer. C) disorder model deployed for the simulations. Note that for the sake of clarity, only the nearest neighbor coupling $J_{n, n\pm 1}$ is shown while in the calculations also non-nearest neighbor interactions are included.

B Calculation of linear absorption and 2DES maps

For the calculation of the linear and third order nonlinear spectra, we calculated the linear and third order nonlinear polarization in the impulsive limit, considering all Liouville pathways that survive the rotating wave approximation. However, for the calculation of induced absorption, we found it sufficient to calculate only the 200 lowest energetic two-excitons for each one-exciton state.³

The experimental 2DES maps are three-dimensional matrices, depending on excitation energy, detection energy, and waiting time. In reference [1], the waiting time dependence of the third order response function has been calculated by considering also Liouville pathways that involve population relaxation (energy transfer) between the second and the third interaction, whereby the probability to find exciton population in state f after time t_2 after it has been created in state i at time t_1 , is given by the two-particle Green's function $G(i, f, t_2)$. The Green's function was found by modified Redfield theory, an approximative perturbative treatment of exciton relaxation. If one were to perform non-linear optimization using this approach, one would have to (i) calculate the Green's function via modified Redfield and (ii) run the complete calculation of all Liouville pathways - including all combinations of energy transfer - over and over again for hundreds of combinations of the fitting parameters, which is prohibitive even on a supercomputer.

For this reason, here we pursue a different approach. For each exciton state e , we calculate only those Liouville pathways that do not involve energy transfer. This avoids the time consuming calculation of the Green's function. What we get is a basis set of pump-probe spectra $\sigma(\omega_3, \omega_f)$ along ω_3 for all f exciton states with energy ω_f in the system. The spectral lineshape for the contribution of each Liouville pathway has been calculated using a phenomenological dephasing parameter of $\Lambda=8$ meV, which resulted from nonlinear optimization and gave best agreement of the tails of experimental and fitted GSA towards low detection energies ω_3 (see Fig. S1a). The Beer-Lambert law for a continuous basis set of absorbing species reads as

$$\Delta T/T(\omega_1, t_2, \omega_3) = -\Delta A(\omega_1, t_2, \omega_3) = d_s \int_{\omega_f} \sigma(\omega_3, \omega_f) \cdot D(\omega_1, t_2, \omega_f) d\omega_f \quad (S5)$$

where the differential transmission $\Delta T/T$ equals the negative of the differential absorption ΔA in the low signal limit, $D(\omega_1, t_2, \omega_3)$, in units of $[\text{cm}^{-3} \text{eV}^{-1}]$, is the exciton distribution function for energies in the range $\{\omega_f, \omega_f + d\omega_f\}$ at time t_2 after excitation with energy ω_1 at time $t_2=0$. and the film thickness is given by d_s . As we know the pump-probe spectrum $\sigma(\omega_3, \omega_f)$, in units of $[\text{cm}^2]$, for all one-excitons, we can find $D(\omega_1, t_2, \omega_f) d\omega_f$ by a simple non-negative least squares fitting using the scipy Python package. In order to keep the number of parameters manageable for a nonlinear optimization, we discretized the active space of one-excitons in the range from 2.09 – 2.135 eV into 9 energy bins. This discretization converts the differential density $D(\omega_1, t_2, \omega_f) d\omega_f$ into the exciton concentration C [in units of cm^{-3}] in the energy bin with mean energy $\overline{\omega_f}$:

$$C(\omega_1, t_2, \overline{\omega_f}) = \int_{\omega=\omega_f-b/2}^{\omega=\omega_f+b/2} D(\omega_1, t_2, \omega_f) d\omega_f \quad (S6)$$

where b is the width of the energy bins. The concentration-time matrix, finally, is related to the two particle Green's function by

$$D(\omega_1, t_2, \omega_f) = \sum_i (D(\omega_1, t_2 = 0, \omega_f) \cdot G(i, f, t_2)) \quad (S7)$$

The initial concentrations $D(\omega_1, i, t_2 = 0)$ of the exciton states can in principle be obtained from the fit of the linear absorption spectrum and the ω_1 spectral distribution.

In a final step, we calculated the transfer matrix (which in the approach of ref. [1] is obtained by modified Redfield theory) by solving a system of ordinary differential equations, as implemented in the scipy package, as described in the main text (eq.2).

Here, we highlight the limitations of this approach, introduced by treating exciton dynamics only in a subsequent step. Our approach treats the excited spectrum $\sigma(\omega_3, \omega_f)$ of excitons at energy ω_f , as independent of time. In doing so, dephasing effects are not rendered. This might lead to artifacts in the exciton density for very early times ($\ll 100\text{fs}$). Moreover, in the calculation of $\sigma(\omega_3, \omega_f)$, the Lorentzian linewidths of all exciton states are all the same, namely the Λ fitting parameter from Table 1 in the main manuscript; while they should differ when their lifetimes are different. This lifetime dependence is however expected to be smoothed out due to the binning procedure that we apply in the above derivation. These limitations are counterbalanced by the high speed of our simulations, reducing the calculation times to just a few hours on a standard laptop computer, thus allowing the study of a multitude of samples in which parameters have been systematically varied.

C Comparison of models

In Figure 1 a of the main text, we show that using our model of non-Gaussian off-diagonal disorder, the best agreement between experimental absorption spectrum and simulation is obtained assuming about 7 defects on a 70-mer. Here, we present a more detailed comparison of experimental and simulated spectra using the first four moments. We normalize the integral of the probe spectrum $S(E)$ to unity, $S_n(E) = S(E) / \int_{E_{max}-0.2eV}^{E_{max}+0.2eV} S_n(E) dE$, E being the probe energy, and E_{max} being the probe energy of maximum absorption. To limit contributions from an incorrect baseline and higher (vibronic or electronic) transitions in the experimental absorption spectrum, we consider only the spectral region close to the absorption maximum in the evaluation of the moments. As the latter depend on these limits, we use the same limits for the moments of the simulated spectra, too. The first moment⁴ is the mean μ :

$$\mu = \int_{E_{max}-0.2eV}^{E_{max}+0.2eV} E \cdot S_n(E) dE \quad (S8)$$

As shown in Fig. S2, the mean μ increases with the number of defects in a roughly linear fashion, while higher amounts of diagonal disorder decrease μ . Note that in Figure S1, the dependence of the mean energy μ on the model parameters has been eliminated by shifting the spectra accordingly to match the simulated μ_{sim} with the experimental one, $\mu_{exp} = 2.109$ eV.

The second centralized moment is the variance. In Figure S1 b, we show the standard deviation σ , which is the positive square root of the variance:

$$\sigma = \left(\int_{E_{max}-0.2eV}^{E_{max}+0.2eV} (E - \mu)^2 \cdot S_n(E) dE \right)^{1/2} \quad (S9)$$

The standard deviation is a measure of the width of the band. As Fig. S2b shows, the width rises with increasing number of defects as well as with increasing diagonal disorder. The experimental value, $\sigma_{exp} = 0.049$ eV, can actually be obtained for any assumed value of defect concentrations or diagonal disorder by adjusting the other one. So, the discussion on whether non-Gaussian off-diagonal disorder is needed to reproduce the experimental absorption spectrum, cannot be based on considering only the width of the band. The important figures of merit are the skewness and “tailedness” (kurtosis) of the band, which are the third and fourth moments, respectively.

The Pearson’s moment coefficient of skewness is defined as the third standardized moment:

$$\gamma = \int_{E_{max}-0.2eV}^{E_{max}+0.2eV} (E - \mu)^3 \cdot S_n(E) dE / \sigma^3 \quad (S10)$$

The skewness of the experimental absorption spectrum is $\gamma_{exp} = 1.0$. In Fig. S2c, we show that none of the simulations reach this high experimental skewness, but the ones with lowest diagonal disorder get closest, attaining skewness values up to 0.85. The reason for the high skewness in the absence of diagonal disorder is the “built-in” skewness of the absorption spectrum of an ideal J aggregate. Although most of the transition strength comes from the lowest energetic exciton state, about 10% derive from higher lying exciton states. The skewness of the band thus depends on the energetic splitting between the lowest and the next higher exciton states, which is a function of exciton

delocalization. Therefore, the standardized skewness (skewness of a band that has been scaled to standard deviation one, see eq. S9) decreases with increasing diagonal disorder, because diagonal disorder adds inhomogenous broadening to the band, which acts more strongly on the standard deviation (Fig. S2b) than on the exciton localization (Fig. S2A).

Finally, the fourth standardized moment is the kurtosis or “tailed-ness” of a band:

$$\kappa = \int_{E_{max}-0.2eV}^{E_{max}+0.2eV} (E - \mu)^4 \cdot S_n(E) dE / \sigma^4 \quad (S11)$$

According to eq. S11, a Gaussian function attains a kurtosis of $\kappa=3$. The kurtosis of the experimental absorption spectrum is $\kappa_{exp} = 5.6$. In Fig. S2d, we show that several combinations of the model parameters yield this experimental kurtosis. The highest kurtosis is found in the absence of both diagonal and off-diagonal disorder; in this case, the Lorentzian lineshapes dominate the kurtosis, being much stronger tailed than a Gaussian.

In summary, we find that several combinations of the model parameters are able to reproduce the width (Fig. S2b) and the tailed-ness (Fig. S2d) of the experimental absorption band, but the high experimental skewness can only be approximately reached when the defect density is between 4 and 8 defects per 70-mer. Therefore, we conclude that the experimental absorption spectrum can only be reproduced when topological defects are present that cause a hard segmentation of the aggregate.

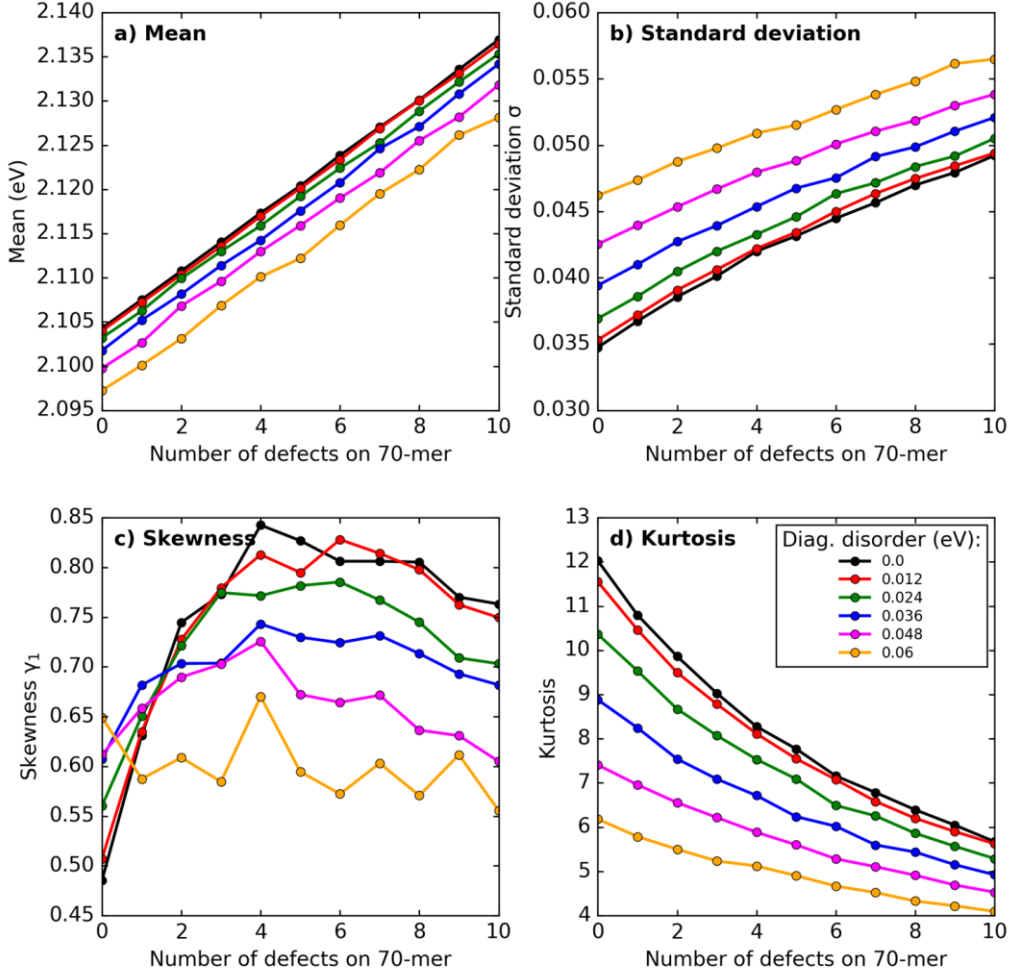


Fig. S2. First, second, third, and fourth moments of the simulated linear absorption spectra, using the model of hard segmentation by defects as explained under point A of this supporting material (panels a, b, c, and d, respectively)

In Fig. S3, we show the result of the simulation of the experimental absorption spectrum by assuming a Lévy distribution of the site energies (diagonal disorder) rather than the couplings (off-diagonal disorder). A symmetric Lévy distribution with mean zero is given by⁵

$$p(E) = \frac{1}{2\pi} \int_{-\infty}^{+\infty} e^{iEt} e^{-(|\beta t|)^\alpha} dt, \quad (\text{S12})$$

where α and β are the index of stability and the scale parameter of the distribution, respectively. As Fig. S3 shows, we do obtain a decent fit also for this model, if we assume both α and β close to 1. However, we find that the fit improves if a 35-mer is calculated instead of a 70-mer, which again shows the need for hard segmentation. Most importantly though, we find that the simulated 2DES spectra, using the best parameters of this model, show negligible strengths of the PA bands and thus completely fail to reproduce the experimental 2DES spectra. For these reasons, we discard this model.

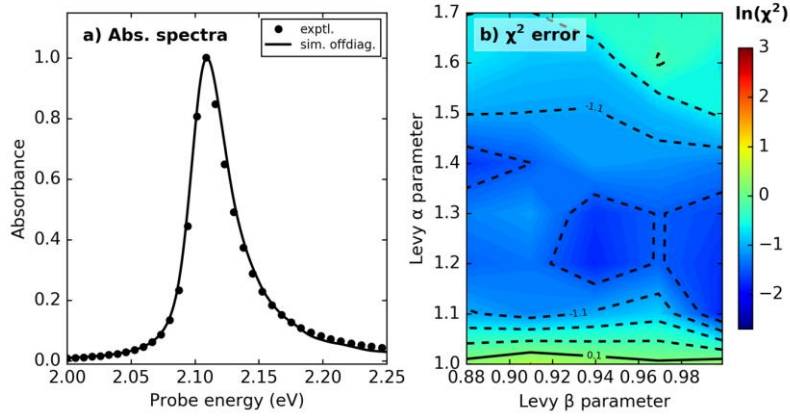


Fig. S3: a) experimental absorption spectrum (dots) and best fit of simulations assuming only diagonal disorder given by a stable symmetric Lévy distribution according to eq. S11 (line). b) The squared error between experiment and simulation, given in a logarithmic color scale (see scale bar) as function of the Lévy parameters.

D Complete results of global fitting

In Fig.S4 a, b, we show experimental 2DES maps at various t_2 times up to 200 fs, the corresponding fits according to eq. S6, and the residuals, in the upper, middle and lower row, respectively. In Fig. S5, we show the same graphs for t_2 times from 370 fs upward. In Fig.S6, we show the time-resolved exciton densities, as obtained from the fits in Fig.S4 in the upper row, while the middle row shows global fits obtained by numerical integration of a system of ordinary differential equations, after nonlinear optimization has been performed on the transfer matrix elements (eq.2 in main text). The lower row shows the residuals. Fig. S7 is the same as Fig.S6, but for longer t_2 times. Fig. S8 gives the transition dipole moment, density of states, and excited state spectra of one-excitons as function of exciton energy. Figures S9, S10, and S11, finally, show exciton densities $C(\omega_1, t_2, \omega_f)$ obtained according to eq. 1 in main text, and fits according to eq.2 in main text (upper and middle rows, respectively) for different pump fluences, as indicated. The lower row shows the residuals.

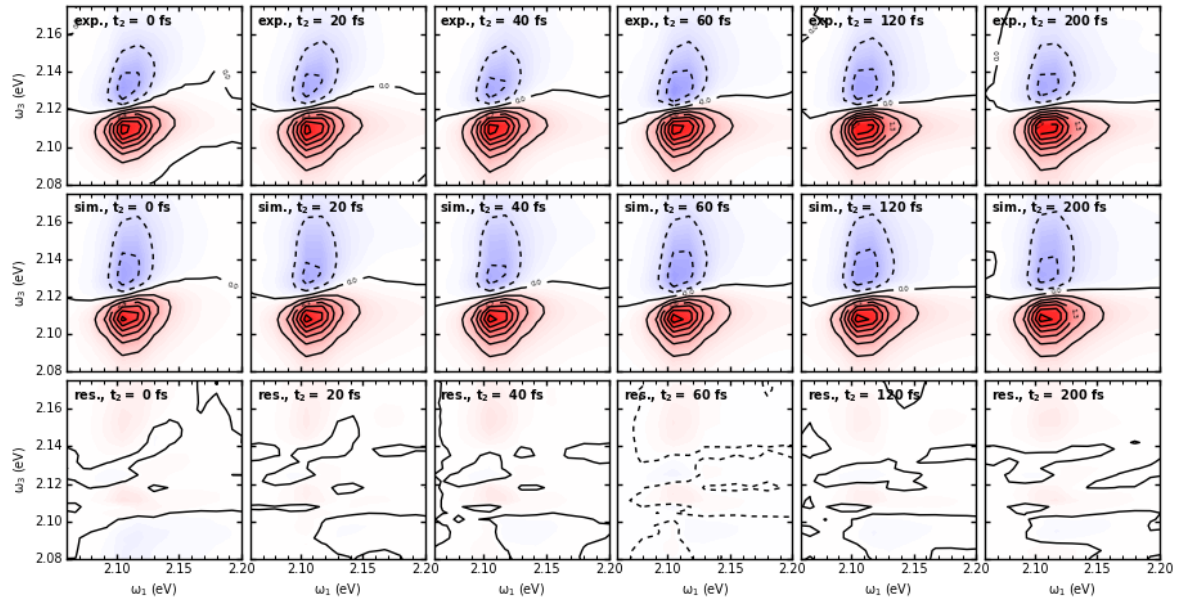


Fig. S4. Experimental 2DES maps, global fits according to eq. S3 using basis states $\sigma(\omega_3, f)$ from a Frenkel exciton model (see Fig. S6), and residuals. (upper, middle, and lower row, respectively)

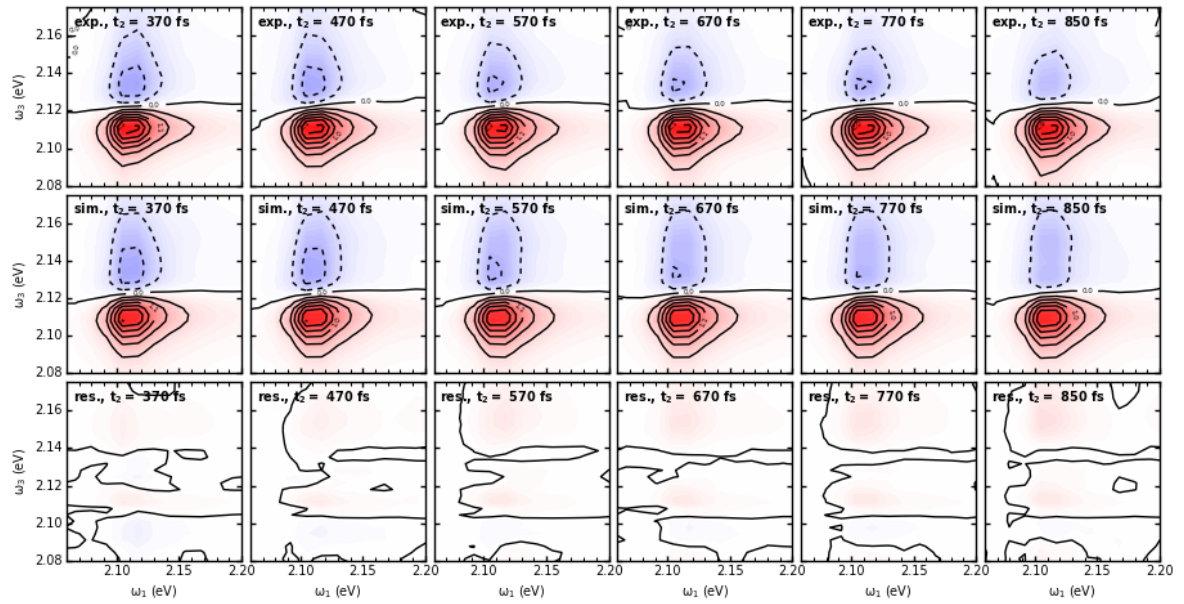


Fig. S5: same as Fig. S4, but for larger t_2 values

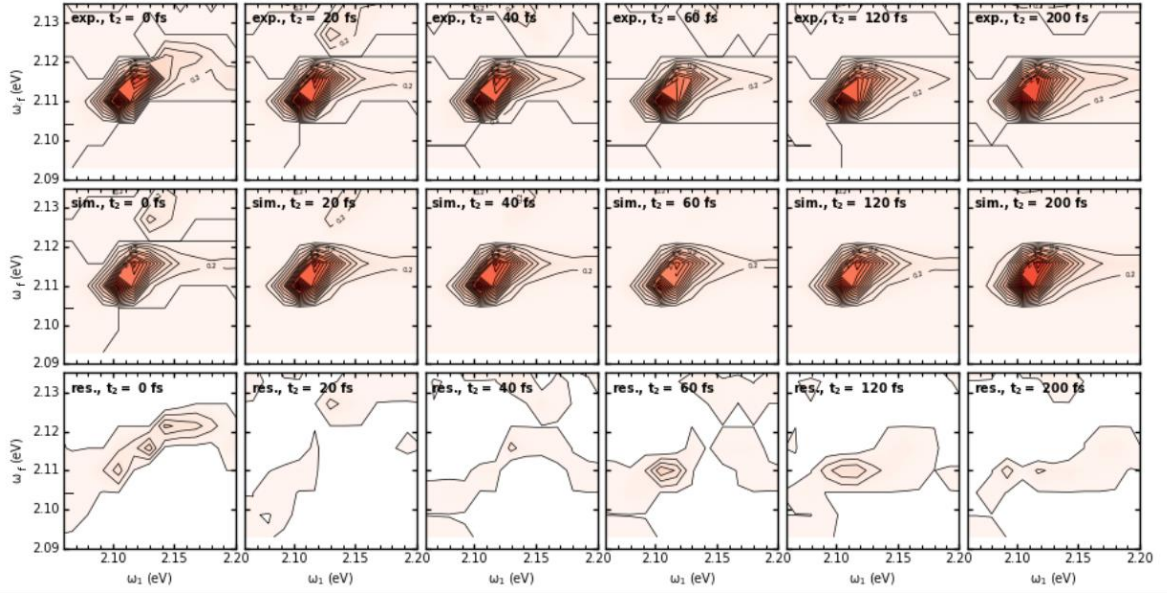


Fig. S6. Time and energy resolved exciton densities $C(\omega_1, t_2, \omega_f)$, as obtained from the global fits in Fig.S4, global fits to $C(\omega_1, t_2, \omega_f)$ by nonlinear optimization of the off-diagonal transfer matrix elements and the dispersiveness parameter γ in eq.2 in main text, and residuals (upper, middle, and lower row, respectively). The false color scale is defined by the maximum signal in the upper row and valid for all three rows.

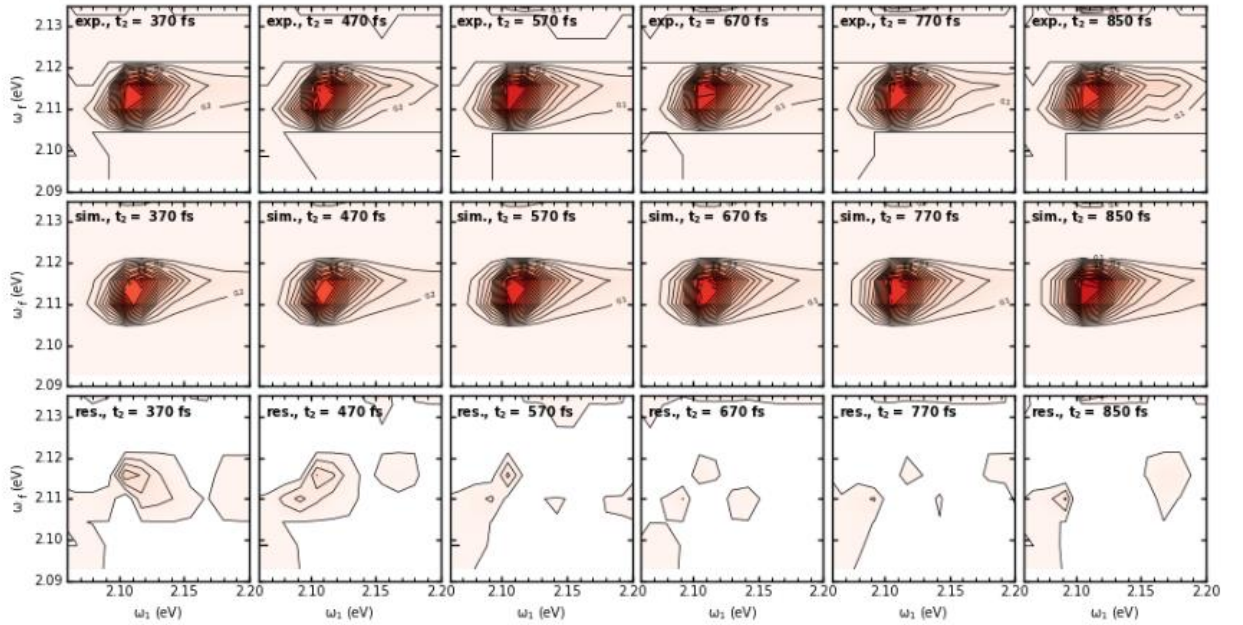


Fig. S7. Same as Fig. S6, but on a longer t_2 scale.

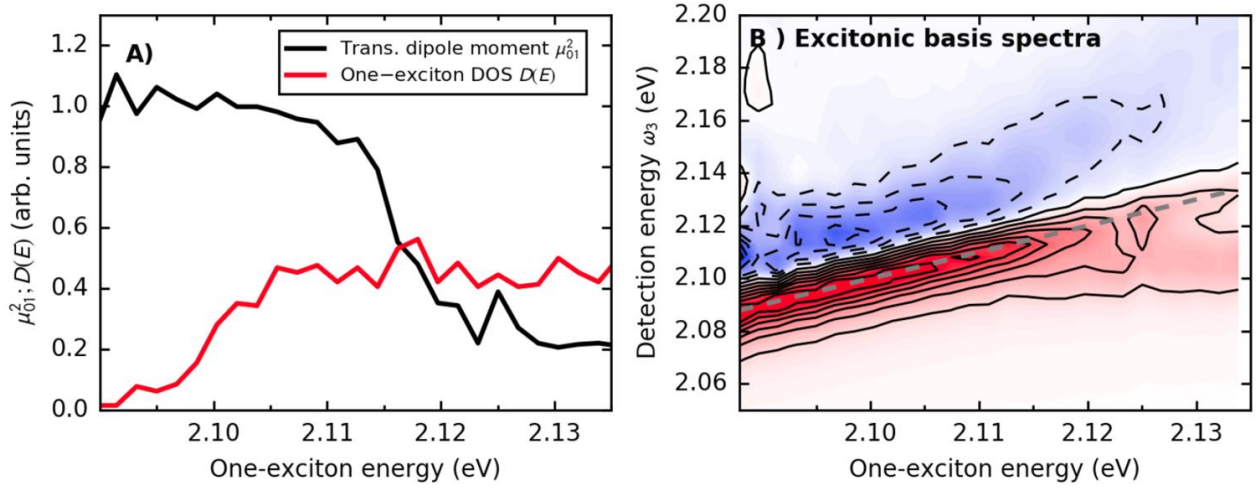


Fig. S8. A) Normalized transition dipole moment for the basis of one-exciton states from the ground state (black) and normalized density of exciton states per energy interval, as function of one-exciton energy. B) Basis spectra $\sigma(\omega_3, f)$ as a function of one-exciton energy, as obtained from calculation of all relevant Liouville pathways starting from the specific one-exciton, normalized to the PB maximum. These states were obtained by diagonalization of a Frenkel Hamiltonian of an aggregate containing Gaussian disorder in the site energies but heavy tail states in the coupling. See Fig.S1C for a pictorial representation of the simulated aggregate. The graph shows that the evolution of the characteristic features of the basis spectra with exciton energy is sufficiently smooth to justify the binning that we have used to reduce the number of basis states in eq. S6.

E Pump fluence dependence

We performed the same analysis on various sets of 2DES maps, varying the pump fluence from 0.3 up to $2.1 \mu\text{J cm}^{-2}$. In Fig. S9, we show the values of the 2DES maps at $\omega_1 = \omega_3 = 2.13 \text{ eV}$ (region of photoinduced absorption) for various times t_2 . Although the pump fluence has been varied by nearly an order of magnitude, the normalized time traces remain very similar. From Fig.S9, we can therefore not confirm the presence of singlet annihilation which has been described in TDBC/water.⁶

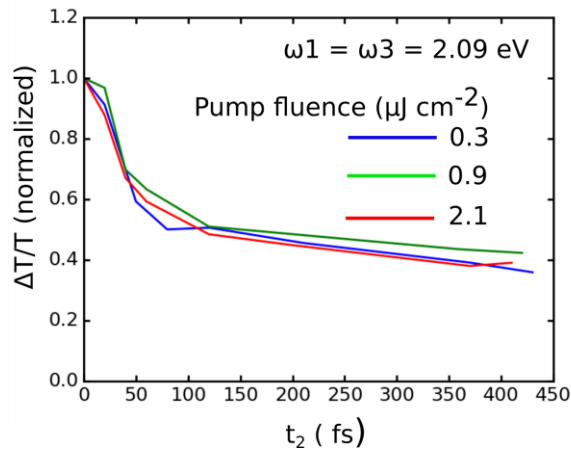


Figure S9. Value of the 2DES maps at the given excitation and detection energy as function of waiting time t_2 . The excitation fluence is parameter.

For the simulations of the intensity dependent 2DES maps, we used the same set of exciton states as in the evaluation according to eq.1 in the main text. The resulting time-resolved exciton distributions are given in Figs S11-13, upper rows. Fitting these with a rate equation model (eq.2 in main text) was possible without systematic deviations, see middle and lower rows for fits and residuals, respectively. The resulting transfer matrices are shown in Fig. S10. They all show similar features as Fig. 4b in main text, namely matrix elements for downward ET which are orders of magnitude faster than those for upward ET. However, increasing the pump intensity leads to an overall reduction of the matrix elements. This finding might be explained by exciton annihilation, being an energy transfer process between two excitons, yielding one exciton in a hot ground state and the other one in a highly excited state. By this mechanism, high energy excitons are constantly “recycled” as long as there is sufficient exciton population, thus yielding an apparent reduction of the overall exciton relaxation rate.

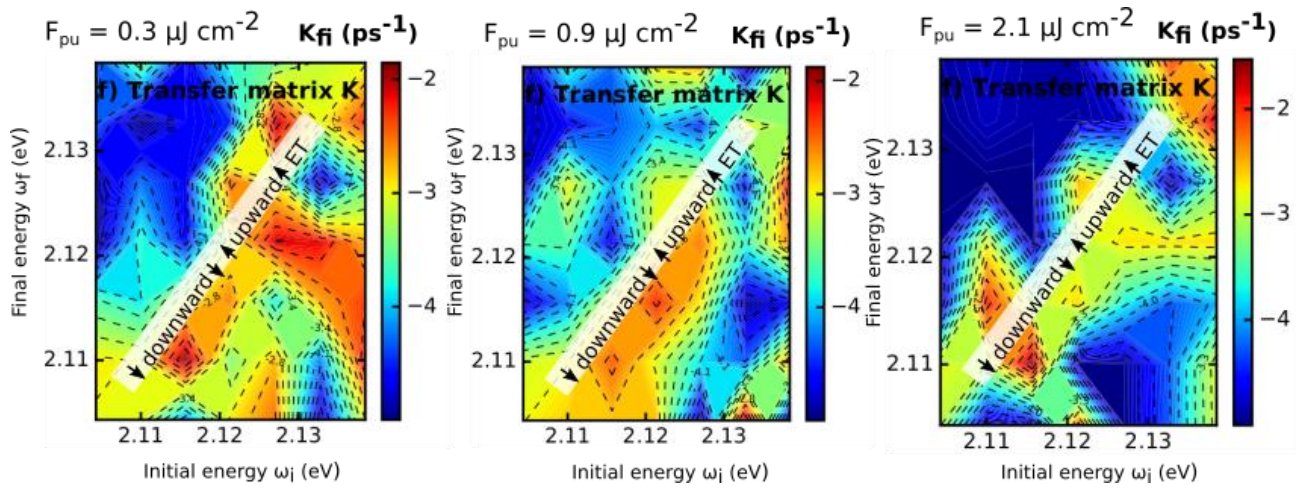


Fig. S10. Transfer matrices K resulting from the fittings in Fig.S11, S12, and S13, using eq. 2 of main text, for measurements analogous to those in Fig.2 of main text at different pump intensities, as given in the legend.

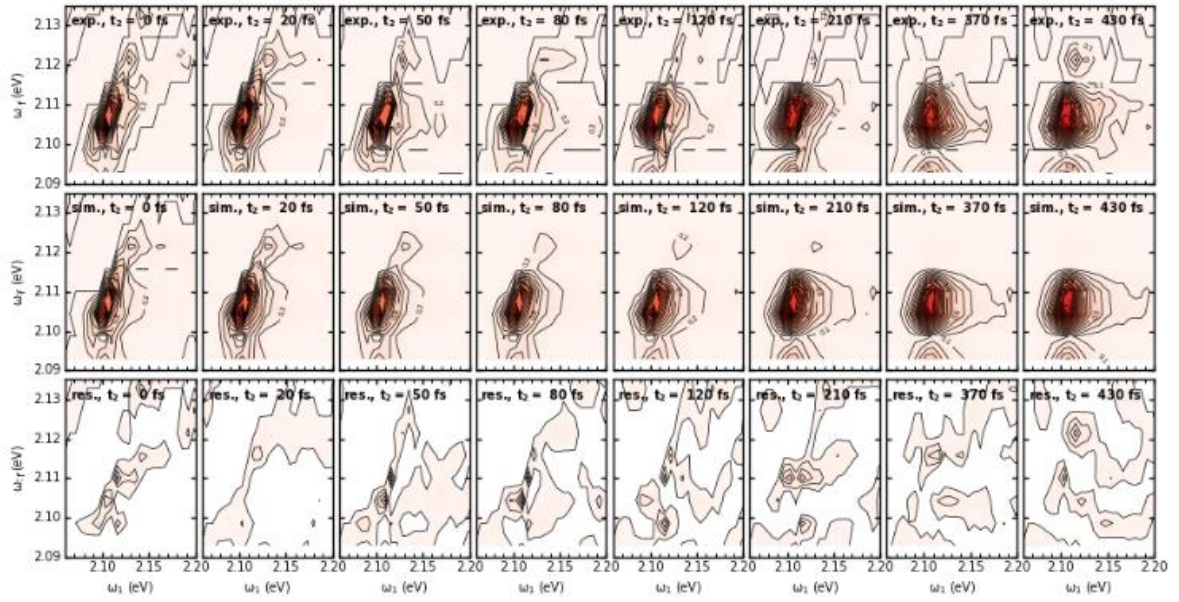


Figure S11: like Fig. S6; pump energy $0.3 \mu\text{J cm}^{-2}$

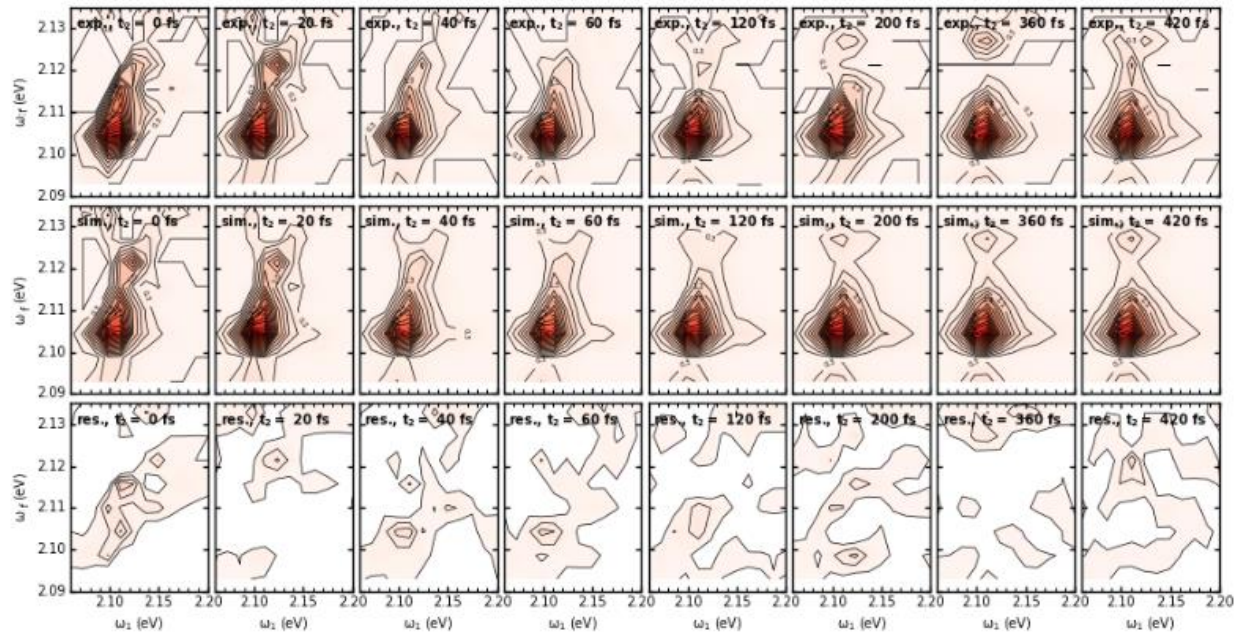


Figure S12: like Fig. S6; pump energy $0.9 \mu\text{J cm}^{-2}$

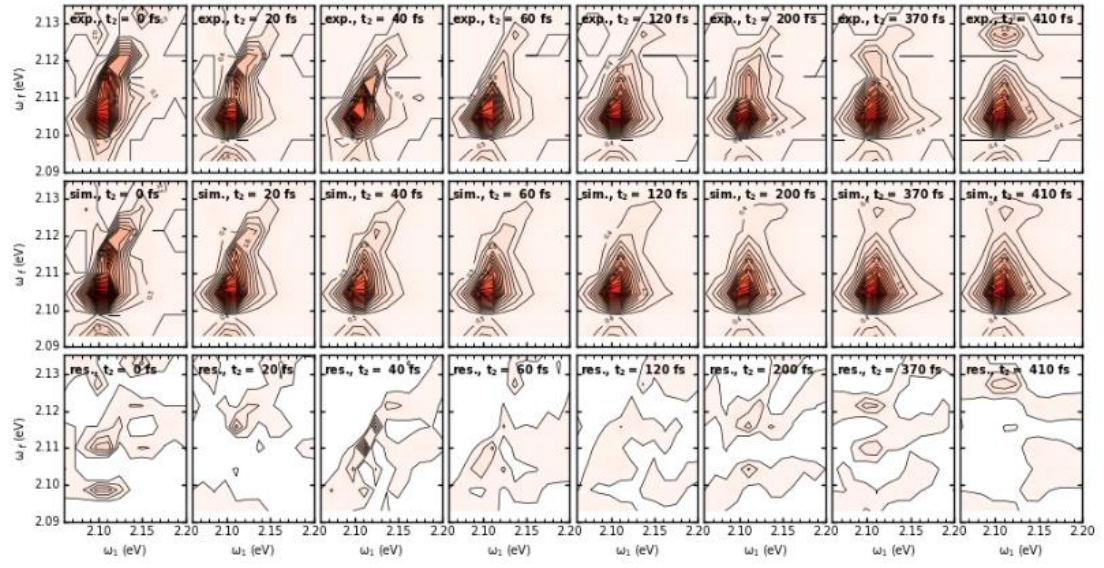


Figure S13: like Fig. S6; pump energy $2.1 \mu\text{J cm}^{-2}$

F Details of Experimental Method:

Two-dimensional electronic spectroscopy was performed in the partial collinear pump-probe geometry employing two collinear phase-locked pump pulses and a non-collinear probe pulse. The probe is delayed by the population time t_2 and its spectrum is measured by a spectrometer. Additionally, a phase-locked pump pulse pair is generated and the two identical pulses are delayed by the coherence time t_1 . The Fourier transform with respect to t_1 allows to resolve the obtained signals with respect to excitation energy. 2DES spectroscopy provides thus the possibility of combining excellent time and spectral precision in excitation and probing.

A broadband non-collinear optical parametric amplifier (NOPA) was used to generate the 10 fs-pump and probe pulses with spectrum spanning the 1.8-2.35 eV range. The NOPA was pumped by 100fs-pulses at 800nm from a regeneratively amplified 1 kHz repetition rate Ti:Sapphire laser (Coherent Libra). To generate coherence delay (T_1), a novel optical device, called TWINS, was used, where the birefringence of α -BBO crystals generates variable delays for pulses polarized along the ordinary and extraordinary axes. As shown in Figure S14, the TWINS setup consists of three blocks A, B and C of two birefringent plates and wedges with their optical axes as shown by yellow arrows. A linear polarizer (1) changes the pump beam polarization from vertically (along the X-axis) to a polarization of 45° with respect to the XY plane. The beam passes through block A which consists of two wedges with optical axis along the Z-axis, the direction of propagation; and Y-axis, respectively. Since the horizontal and vertical components of the pump beam propagate with different velocities depending on the different refractive indexes, they are delayed by t_1 . By moving the entire block A, it is possible to scan the delay t_1 . Due to the different refraction for the X- and Y- pulses at the interfaces, the pulses are not collinear and their phase fronts are not parallel after passing through block A. In order to correct these features, block B is inserted in the path. It is composed of two wedges identical to those in block A but placed in the opposite order. Block C, whose optical axis is along the X-axis, introduces a constant negative delay. After passing through the second linear polarizer (2), the two orthogonal and delayed pump pulses are both polarized at 45° with respect to the XY plane.

The birefringent material introduces a positive dispersion to the pump pulses which is compensated by a pair of chirped mirrors. The pump pulses are compressed to near transform limit by adjusting the number of reflections at the chirped mirror pair. The pump pulses then pass through a chopper working at a frequency of 500 Hz.

The t_1 delay and phase between the two pump pulses are calibrated by translating block A and observing the interference fringes of the beams scattered by a pinhole at the sample position into the spectrometer. The pump delay and phase are monitored in parallel to data acquisition and the subsequent t_1 scans by deviating a small part of the pump beams into a photodiode and acquiring their interference.

The probe pulse dispersion is compensated by another pair of chirped mirrors. The population delay (t_2) between the pump and probe pulses is controlled by another pair of mirrors on a translation stage. The interference between the scattered pump pulses and the probe pulses is minimized by using an audio speaker changing the optical path of the probe beam.

The probe pulses are delayed by the population time t_2 with a conventional translation stage. Pump and probe pulses are focused to a spot size of 50 μm onto the sample at a small angle using all-reflective optics. The probe pulses transmitted through the sample are spectrally dispersed in a monochromator and recorded with a multichannel detector acquiring all laser shots at 1 kHz. For a fixed value of the population time t_2 , the differential transmission (DT/T) spectrum $\text{DT}/T(t_1, t_2, \omega_3)$, ω_3 being the probe frequency, is recorded as a function of the coherence time t_1 . Finally, the absorptive 2DES spectrum $\text{DT}/T(\omega_1, t_2, \omega_3)$ is obtained by taking the Fourier transform with respect to the coherence time t_1 . Along the excitation energy axis ω_1 we normalize the signal such that the “photobleach excitation spectra” after long times (i.e, one-dimensional spectra $\text{DT}/T(\omega_1, t_2=400 \text{ fs}, \omega_3=2.10 \text{ eV})$) approximately match the ground state absorption spectrum.

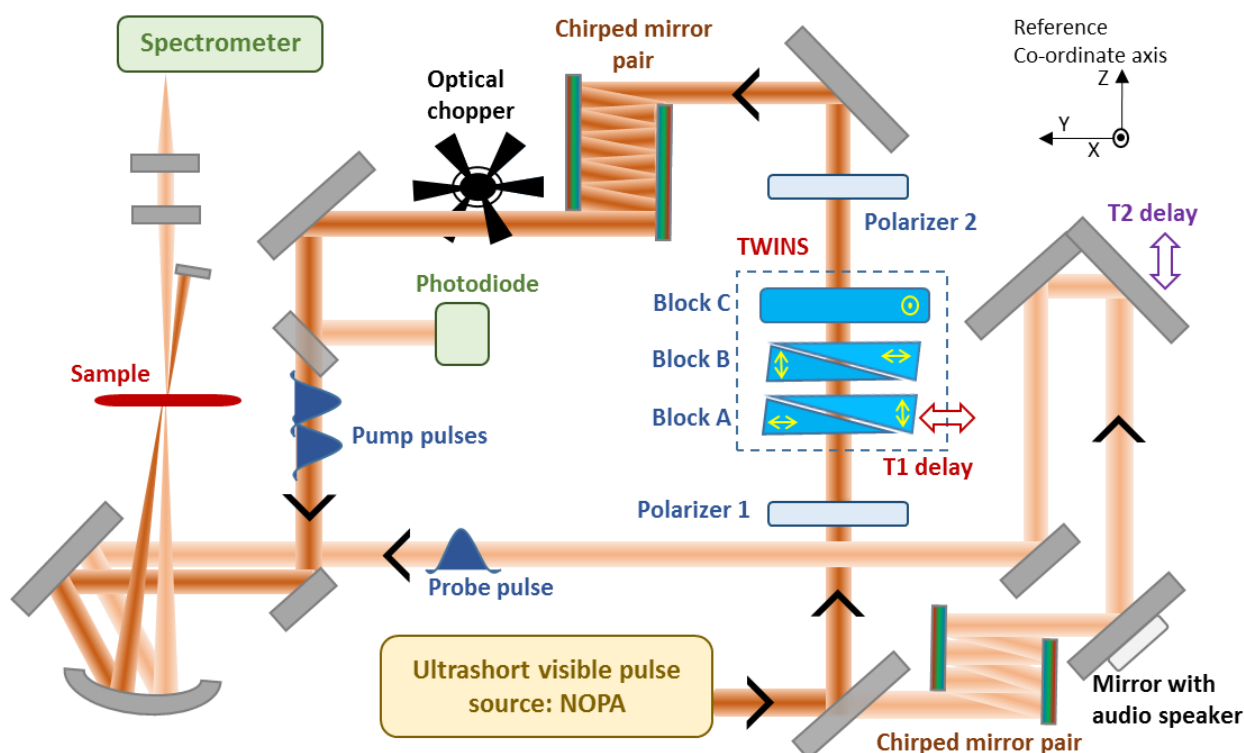


Fig. S14. Experimental set up for 2DES

REFERENCES:

- ¹ Stiopkin, I.; Brixner, T. Yang, M.; Fleming, G. R. Heterogeneous Exciton Dynamics Revealed by Two-Dimensional Optical Spectroscopy, *J. Phys. Chem. B* **2006**, *110*, 20032-20037.
- ² Johansson, J. R.; Nation, P. D.; Nori, F. QuTiP 2: A Python framework for the dynamics of open quantum systems, *Comp. Phys. Comm.* **2013**, *184*, 1234
- ³ Dijkstra, A. G.; Jansen, T. L. C.; and Knoester, J. Localization and coherent dynamics of excitons in the two-dimensional optical spectrum of molecular J -aggregates, *J. Chem. Phys.* **2008**, *128*, 164511.
- ⁴ For the definition of moments, see [https://en.wikipedia.org/wiki/Moment_\(mathematics\)](https://en.wikipedia.org/wiki/Moment_(mathematics))
- ⁵ Feller, W. An Introduction to Probability Theory and Its Applications (Wiley, New York, 1966).
- ⁶ Van Burgel, M.; Wiersma, D. A.; Duppen, K. The Dynamics of One-Dimensional Excitons in Liquids. *J. Chem. Phys.* **1995**, *102*, 20.